https://doi.org/10.5194/egusphere-2026-4709
Preprint. Discussion started: 2 September 2026

Quantitative constraints on secondary ice production in stratiform mixed-phase clouds using synergistic lidar-radar observations

Dongzhe Jing[1,2,3], Kaiming Huang[1,2,3*], Yun He[1,2,3*], Fan Yi[1,2,3], Rang Cao[1,2,3], Fangzheng Cheng[1,3], He He[1,2,3]

[1]School of Earth and Space Science and Technology, Wuhan University, Wuhan, China.
[2] National Field Observation and Research Station (Hubei Wuhan) for Atmospheric Remote Sensing, Wuhan, China.
[3] Key Laboratory of Geospace Environment and Geodesy, Ministry of Education, Wuhan, China.

Correspondence to: Kaiming Huang (hkm@whu.edu.cn), Yun He (heyun@whu.edu.cn)

Abstract. Secondary ice production (SIP) remains a major source of uncertainty in numerical models, particularly for single-layer, stratiform mixed-phase clouds (MPCs), owing to limited quantitative microphysical observations in nature. These clouds, consisting of a supercooled liquid layer and ice virgae below, provide an ideal natural laboratory for investigating cloud microphysical processes. We analyzed the ice multiplication factor (IMF) from 11 stratiform MPC cases based on lidar-radar synergistic observations and advanced retrieving approach associated. IMF was calculated as the ratio of the ice crystal concentration at 180 m below the base of supercooled liquid layer, to the ice nucleating particle concentration at cloud-top level. Two typical cases with different temperatures in supercooled liquid layer (T_{SL}) were studied. The first case was relatively warm with T_{SL} of -6.8 ~ -6.3 ℃, showing a relative high IMF of 36.2; while, the second one was colder with T_{SL} of -10.6 ~ -8.7 ℃, exhibiting a much lower IMF of about 3.0. For statistics, the IMF exhibits a distinct temperature dependence, remaining close to 1 when the T_{SL} is below -8 ℃, and increasing to 351.8 as the T_{SL} approaches -5 ℃. Additionally, Stronger SIP was associated with smaller ice particles above -8 ℃, with a Pearson correlation coefficient of -0.73 between the IMF and the particle maximum diameter. These findings suggest the Hallett–Mossop process plays a significant role in SIP under relatively warm conditions, providing an invaluable observational constraint for improving SIP representations in numerical weather prediction and global climate models.

https://doi.org/10.5194/egusphere-2026-4709
Preprint. Discussion started: 2 September 2026

1 Introduction

Single-layer, shallow stratiform mixed-phase clouds (MPCs) remain one of the largest sources of uncertainty in numerical weather prediction and global climate models, because their radiation properties are highly sensitive to cloud phase (Korolev, 2017). Secondary ice production (SIP), defined as the number concentrations of ice crystals rapidly enhanced in the presence of preexisting ice without involvement of additional ice nucleating particles (INPs), can substantially enhance ice-phase-relevant microphysical processes within clouds (Korolev et al., 2020; Korolev and Leisner, 2020), and thus plays an essential role in cloud electrification and precipitation efficiency (Field et al., 2017).

The intensity of SIP is generally reflected by ice crystal number concentration (ICNC) that exceeds the INP concentration (INPC) by one or more orders of magnitude. The ice multiplication factor (IMF=ICNC/INPC) provides a direct quantitative measure of ice multiplication level by linking primary ice formation to secondary ice amplification, and thus serves as a key metric for evaluating SIP intensity. However, existing SIP parameterizations are primarily based on laboratory experiments (Luke et al., 2021), which may not fully represent the complexity of SIP in natural clouds. Therefore, the efficiency of SIP in MPCs remains poorly quantified from observations. Moreover, a recent study highlighted that the high sensitivity of SIP to model setups and environmental conditions poses a major challenge for its representation in numerical models (Raatikainen et al., 2026).

These modelling challenges are directly reflected in the ongoing controversy over which SIP mechanism, e.g., rime splintering (so-called Hallett–Mossop process, i.e. HM process), fragmentation of ice-ice or ice-droplet collision, or shattering of large supercooled droplets during their freezing (Korolev and Leisner, 2020), dominates in natural single-layer stratiform mixed-phase clouds. Among them, the HM process is the most widely represented type in numerical models (Field et al., 2017). Some studies held the view that the HM process alone is insufficient to explain the high ICNC values of $10^{-1} \sim 10^{1}$ L^{-1} measured by airborne in situ observations in stratiform MPCs with cloud-top temperature (CTT) warmer than -10 °C (Sotiropoulou et al., 2020; Yang et al., 2020), and they instead proposed that other potential SIP mechanisms must also participate in ice multiplication. However, Raatikainen et al. (2026) suggested that the commonly used default parameterization of the HM process may underestimate secondary ice production under certain conditions. Their large-eddy simulations indicated that the HM process could be substantially more efficient in warm stratiform mixed-phase clouds than represented by the default model configuration. These contradictory conclusions underscore the lack of quantitative observational constraints on SIP efficiency in natural clouds.

A major limitation of current observational studies is the difficulty in quantifying both the INPC and ICNC in the same MPC. Many previous investigations of SIP processes in natural MPCs relied on airborne in situ measurements, which offer the advantage of directly sampling ice crystals. However, Korolev and Leisner (2020) pointed out that the concentration of small ice crystals may be overestimated due to the particle shattering effect when using a 2D-S probe, potentially leading to a misjudgment of SIP contributions. In addition, airborne observations are relatively scarce and generally unable to characterize the vertical structure of cloud layers (Wang et al., 2024), resulting in limited spatial and temporal coverage. In

https://doi.org/10.5194/egusphere-2026-4709
Preprint. Discussion started: 2 September 2026

addition to in situ measurements, the millimeter cloud radar (MMCR) has been widely used to investigate SIP, because it provides vertically resolved retrievals of microphysical parameters within MPCs and is capable of penetrating optically-thick clouds (Li et al., 2021; Luke et al., 2021). Since radar reflectivity is jointly determined by both the size and number concentration of the targeting particles, retrievals of ICNC from MMCR alone remain subject to substantial uncertainty; moreover, MMCR observations cannot provide the information on the ice nucleating particle concentrations (INPC), making it difficult to alone quantify the efficiency of SIP.

To address this gap, we develop a synergistic ground-based remote-sensing framework that combines polarization lidar with a Ka-band MMCR. Polarization lidar offers unique capabilities of discriminating cloud phase (Cheng and Yi, 2020; Yi et al., 2021, 2024) and estimating the INPC in the surrounding cloud-free regions (Shen et al., 2024; He et al., 2025). Owing to their distinct operating wavelengths, lidar and MMCR detect ice crystals (10^1 ~ 10^3 μm, Coutris et al., 2017) in the Mie and Rayleigh scattering regimes, respectively. Lidar-derived particle extinction is approximately proportional to particle projected area, while MMCR reflectivity is generally proportional to the sixth power of the particle size, providing complementary constraints on ice crystal size and number concentration (Bühl et al., 2019). By combining these complementary observations, the proposed lidar-radar framework enables simultaneous estimates of both ICNC and INPC in single-layer, shallow stratiform MPCs, allowing for one of the first quantitative assessments of IMF under natural atmospheric conditions.

A polarization lidar and a Ka-band millimeter cloud radar have been deployed at the National Field Observation and Research Station for Atmospheric Remote Sensing in Wuhan University (30.5°N, 114.4°E) (Yi et al., 2024; Zhang et al., 2025). This integrated observing strategy enables quantitative estimation of the ice multiplication factor (IMF), providing an observational constraint on secondary ice production that is difficult to obtain using a single remote-sensing instrument alone. Through long-term measurements of shallow stratiform mixed-phase clouds over central China, we quantify IMF under natural atmospheric conditions and, on this basis, discuss the SIP mechanisms. The paper is organized as follows. Section 2 provides a brief description of the instruments and data processing methods. Section 3 presents two contrasting case studies that demonstrating a distinct temperature dependence of SIP. In Section 4, statistical results for 11 cases are presented. Finally, in the last section, conclusions are presented.

2 Data and method

2.1 532-nm Polarization Lidar data

A 532-nm polarization lidar has been employed at Wuhan University (30.5°N, 114.4°E) since 2010. Routine observation of aerosols and clouds has been carried out to analyze the aerosol-cloud interaction. The lidar system was described in detail by Kong and Yi (2015). Raw data are stored with resolutions of 1 min and 30 m. The volume depolarization ratio (VDR) is defined as the ratio of perpendicular- to parallel-oriented signals, multiplied by the gain ratio, which is used to convert into the particle depolarization ratio (PDR) (Freudenthaler et al., 2009). The particle backscatter coefficients (BSC) of aerosols

https://doi.org/10.5194/egusphere-2026-4709
Preprint. Discussion started: 2 September 2026

and ice crystals are retrieved by Fernald method (Fernald, 1984), by assuming a fixed lidar ratio of 50 sr (Müller et al., 2007) and 20 sr (O'Connor et al., 2004), respectively. The particle extinction coefficient (E) for ice crystals is multiplied by particle backscatter and a larger lidar ratio of 32 sr, compensating for the multiple scattering effect by ice crystals (Seifert et al., 2007).

2.2 Ka-Band MMCR data

The Ka-band MMCR at Wuhan University is a dual-polarization frequency-modulated continuous-wave Doppler radar, which has been employed near the lidar. The detailed descriptions of MMCR are presented in previous studies (Mao et al., 2023; Cao et al., 2025). The measured reflectivity factor (Z) is stored with a vertical resolution of 30 m and a temporal resolution of 0.26 s (0.104) for non-precipitation (or precipitation) conditions. In this study, data are processed into 1-min average values to fit the observations of lidar. The detectable minimum Z of MMCR can reach approximately -46 dBZ at 5 km and -40 dBZ at 10 km (Fang et al., 2025). The retrieval method of ice water content (IWC) followed the study by Hogan et al. (2006), with an error within 50% when T > -40℃ (Hogan et al., 2006).

2.3 ERA5 reanalysis data

The European Center for Medium-Range Weather Forecasts (ECMWF) reanalysis version 5 (ERA5) is an atmospheric reanalysis field of global climate from 1940 onwards, providing the hourly estimates of atmospheric, land, and oceanic climate variables in 0.25° × 0.25° horizontal grids at 37 pressure levels (Hersbach et al., 2020; Hersbach et al., 2023). In this study, the temperature data at (30.5°N, 114.5°E) are used to estimate the atmospheric conditions and calculate the INPC.

2.4 INPC retrieval method

The lidar-derived cloud-free aerosol extinction coefficient profiles obtained before or after the presence of clouds are used to calculate the INPC. First, the dust (E_d) and non-dust (E_{nd}) extinction coefficients are separated by the polarization-lidar photometer networking (POLIPHON) method, by assuming the PDR of 0.31 for dust and 0.05 for non-dust (Tesche et al., 2009). Over Wuhan, the non-dust component is assumed to consist predominantly of continental aerosol (Jing et al., 2025); thus, 'E_c' will be used to represent 'E_{nd}' in the following.

Subsequently, the number concentration ($n_{250,\mathrm{d,dry}}$) of large dust (continental, $n_{250,\mathrm{c,dry}}$) aerosol particles (radius > 250 nm) are estimated by multiplying E_d and corresponding $c_{250,\mathrm{d}}$=0.18 Mm cm^{-3} (E_c and corresponding $c_{290,\mathrm{c}}$=0.10 Mm cm^{-3}) (Mamouri and Ansmann, 2016; He et al., 2023). For continental aerosol, the subscript '290' of $c_{290,\mathrm{c}}$ takes into account the effect of potential water uptake by particle hygroscopic growth (Mamouri and Ansmann, 2016). Finally, INPC was calculated by using the immersion-freezing parameterizations proposed by D15 for dust (DeMott et al., 2015) and D10 for continental aerosol (DeMott et al., 2010),

$$n_{\mathrm{INP,d,D15}}(z) = 3 \times n_{250,\mathrm{d,dry}}(\mathrm{z})^{1.25} \times \exp\left[0.46 \times \left(273.16 - T(z)\right) - 11.6\right] \quad (1)$$

https://doi.org/10.5194/egusphere-2026-4709
Preprint. Discussion started: 2 September 2026

$$n_{\mathrm{INP,c,D10}}(z) = 5.94 \times 10^{-5} \times [273.16 - T(z)]^{3.33} \times n_{\mathrm{250,c,dry}}(z)^{[0.026\times(273.16-T(z))+0.0033]} \quad (2)$$

where T refers to temperature in units of K and is obtained from ERA5 data. Given that D10 and D15 are developed based on laboratory conditions of pressure P_0 =1013 hPa and temperature T_0 =273.16 K (DeMott et al., 2010, 2015), the retrieved INPC is corrected by multiplying $(T_0 \cdot P(z))/(T(z) \cdot P_0)$ in different atmospheric conditions (Mamouri and Ansmann, 2015).

D15 (D10) parameterization is generally suitable for the temperature range of -35 ~ -21 ℃ (-35 ~ -9 ℃). Wieder et al. (2022) extrapolated the applicability of D10 and D15 to temperatures as high as -5 ℃, and found that the uncertainties of INPCs at -20 ~ -5 ℃ between lidar-retrieval and in-situ measurements were within an order of magnitude.

2.5 ICNC retrieval method

The LIRAS-ice method is used to estimate the ICNC in ice virga region, based on profiles of MMCR-measured reflectivity factor Z and lidar-derived particle extinction coefficient E for ice virga. This method is introduced by Bühl et al. (2019).

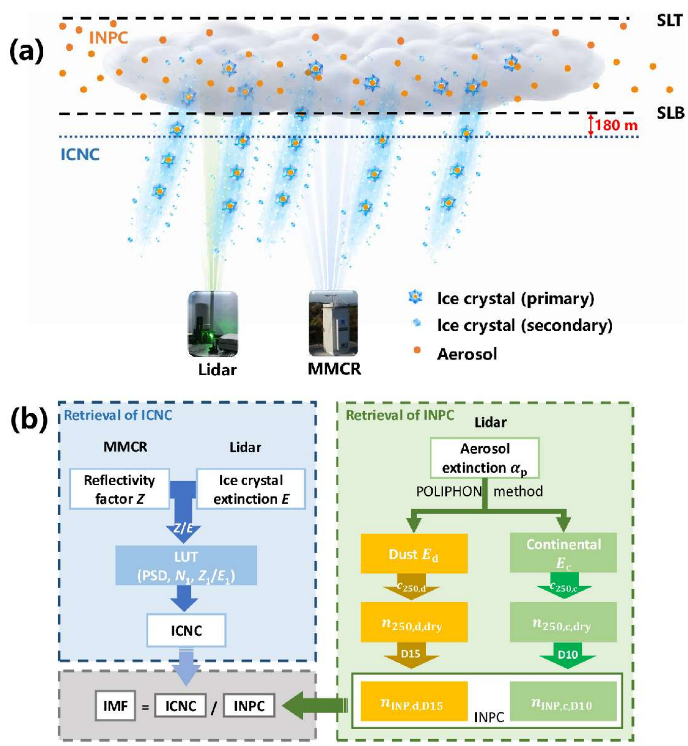

https://doi.org/10.5194/egusphere-2026-4709
Preprint. Discussion started: 2 September 2026

Figure 1. (a) Schematic diagram of mixed-phase cloud joint observation by lidar and MMCR. (b) Flowchart of INPC and ICNC retrieval.

First, a look-up table (LUT) is established, which contains groups of numerical particle size distribution (PSD), normalized reflectivity (Z1), extinction coefficient (E1), and ICNC (N1). These variables are uniquely linked through the PSD, which is parameterized as a function of the median value of particle maximum diameter (Dm). The Z1-to-E1 ratio and Dm can be established for various ice crystal habits. Then, by comparing the observed Z-to-E ratio by the joint lidar and MMCR measurements with the numerical Z1-to-E1 ratio, the best-fit Dm and N1 are determined. Finally, the actual ICNC is obtained through best-fit N1 multiplied by a scaling factor of Z/Z1 or E/E1.

Throughout the whole process, ice crystal shapes are regarded as column-like at T > -8 ℃, plate-like at T of -12 ~ -8 ℃ and -35 ~ -18 ℃, sector branched at T of -18 ~ -12 ℃ (Bailey and Hallett, 2009). The parameterization parameters for each ice crystal shape are presented in Appendix A of Bühl et al. (2019). The uncertainties for both INPC and ICNC are estimated to be a factor of 3 (Mamouri and Ansmann, 2016, 2017; Ansmann et al., 2019; He et al., 2025). The schematic diagram of the joint lidar and radar observation on single-layer stratiform MPC, as well as retrieval procedures for INPC and ICNC, are presented in Fig. 1.

3 Results

3.1 Case 1 on 15 November 2025: remarkable ice multiplication

Fig. 2a-c shows the single-layer stratiform MPC from lidar and MMCR observations on 15 November 2025. The missing data in White between 23:07 and 23:09 in Fig. 2a and 2b might be due to dew condensed on the roof window that the laser pulses pass through (Yi et al., 2021), and the missing MMCR data was caused by the radar self-check at 23:01 and the radar malfunction after 23:07. It can be noted that the MPC occurred from about 22:35 LT, with a shallow supercooled liquid layer at 4.44-4.65 km and an ice virga region below this layer, and the CTT was -6.8 ℃. The top of the supercooled liquid layer (SLT) was identified at approximately 4.65 km from the reflectivity factor (Z) of MMCR (Fig. 2c); and its base (SLB) was clearly distinguished as 4.44 km, based on the minimum value of volume depolarization ratio (VDR) due to the incident light beam entering the supercooled liquid layer rich in small water droplets from the ice virga region (Fig. 2b). The very large values of range-corrected signal (RCS) and VDR within the supercooled liquid layer were caused by the strong backscattering and multiple scattering effects of high concentration droplets (Yi et al., 2024), respectively.

At the SLT, primary ice crystals were first formed through heterogeneous nucleation owing to lower temperatures. During the fall, these ice crystals may grow through the Wegener–Bergeron–Findeisen (WBF) process, riming with supercooled liquid droplets, or ice aggregation (Ávila et al., 2009; Storelvmo and Tan, 2015). Subsequently, ice crystals sedimented out of the supercooled liquid layer; nevertheless, they completely sublimated before reaching the 0° level (Bühl

https://doi.org/10.5194/egusphere-2026-4709
Preprint. Discussion started: 2 September 2026

et al., 2016), forming a long ice virga. The rectangle in Fig. 2a-c represents the strong ice virga region at about 3.74-4.44 km between 22:44-23:07 LT.

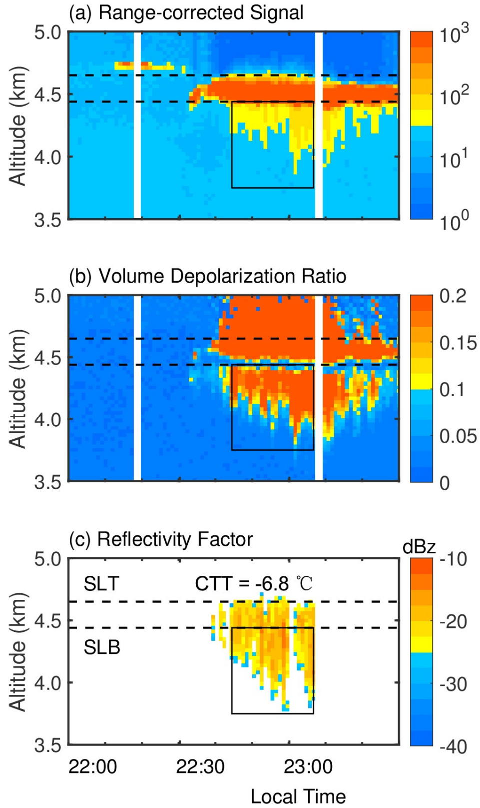

Figure 2. Lidar and MMCR observations of an MPC during 22:30-23:30 LT on 15 November 2025. Time-height contour sections of (a) RCS, (b) VDR, and (c) Z. The dashed lines represent the top and base of the supercooled liquid layer. The solid rectangles represent the ice virga region of our concern during 22:44-23:07 LT.

We calculated the averaged optical and microphysical parameters in the period of 22:44-23:07 LT derived from the lidar and MMCR measurements (Fig. 3a-c). When the ice crystals fell about 90 m from the SLB, the mean backscatter coefficient (BSC) rapidly decreased to about 4.4 Mm^{-1} sr^{-1} from far more than 10 Mm^{-1} sr^{-1}, and the VDR increased to 0.24 from a small value of 0.05 at the SLB. As the height descended, the BSC, VDR, and the IWC kept decreasing due to the sublimation of ice crystals, which was consistent with the previous observation of ice virga (Cheng and Yi, 2020; Yi et al., 2024).

https://doi.org/10.5194/egusphere-2026-4709
Preprint. Discussion started: 2 September 2026

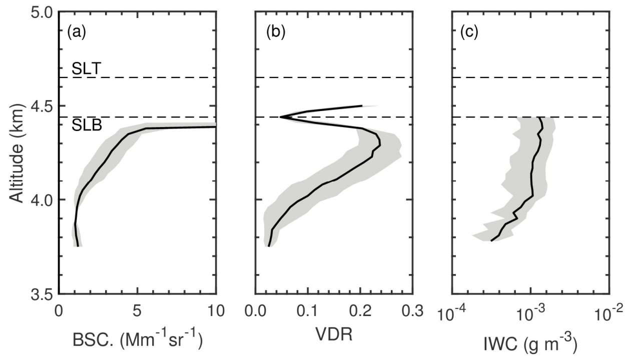

Figure 3. Profiles of averaged (a) BSC, (b) VDR, and (c) IWC in 22:44-23:07 LT. Shadows represent the values of standard deviation. The dashed lines represent the top and base of the supercooled liquid layer.

The VDR, particle depolarization ratio (PDR) and BSC for the dust and continental aerosols were derived from the lidar measurements in 22:00-22:10 LT before the presence of the MPC (Fig. 4a and 4b), and then we calculated the number concentrations of dust and continental particles as the INPs (INPCd and INPCc, Fig. 4c). The D10 and D15 INPC parameterizations were adopted for continental and dust aerosols (DeMott et al., 2010, 2015), respectively, described in detail in the Section Method. At the height of the SLT, the INP population was dominated by continental aerosols with BSC of approximately 1.0 Mm^{-1} sr^{-1}, corresponding to INPCc of 0.03 L^{-1} (Fig. 4c).

We estimated the ICNC by following the LIRAS-ice (LIdar RAdar Synergy—retrieval of ice microphysical properties) method (Bühl et al., 2019). Considering the relatively warm temperature in the supercooled liquid layer of -6.8 ~ -6.3 ℃ at 23:00 LT, the ice shape can be regarded as column-like based on the relationship between ice crystal morphology and temperature (Bühl et al., 2016; Li et al., 2021), and accordingly, the average ICNC was derived from the combined observations of lidar and MMCR between 22:44-23:07 LT (Fig. 4c). As the height decreased, the ICNC dropped rapidly to about 10^0 L^{-1} from a large value of 10^2 L^{-1} near the SLB due possibly to the residual supercooled water droplets. Here, the ICNC at a height of 180 m below the SLB was used as the indicator of ice crystals produced in the supercooled liquid layer. The value of 180 m was chosen to ensure that no supercooled water droplets are present and the ice crystals are minimally affected by sublimation or aggregation processes as far as possible (Bühl et al., 2016), which was demonstrated to be an effective method through a sensitivity test (He et al., 2025). As a result, the ICNC at 180 m below the SLB was 1.10 L^{-1}, which was 36.2 times larger than the INPCc.

https://doi.org/10.5194/egusphere-2026-4709
Preprint. Discussion started: 2 September 2026

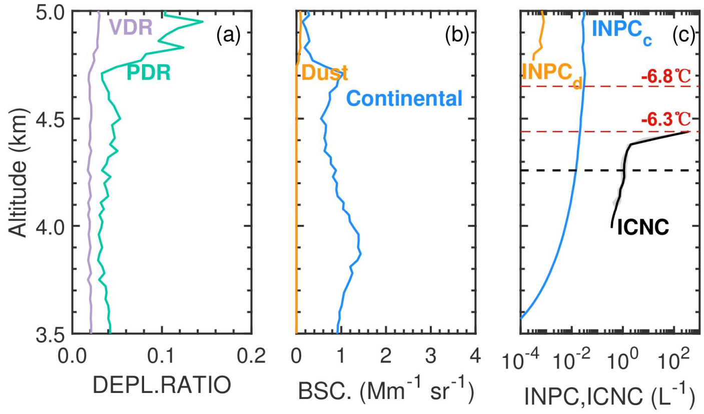

Figure 4. Profiles of (a) VDR and PDR, (b) continental and dust aerosol BSC in 22:00-22:10 LT, and (c) INPC for continental and dust aerosols in 22:00-22:10 LT and ICNC for ice virga in 22:44-23:07 LT. In Fig.4c, the dashed horizontal red lines represent the SLT and SLB, respectively, and the dashed horizontal black line represents 180 m below the SLB.

Now that the uncertainties in both the INP parameterization and ICNC retrieval are approximately a factor of 3 (Mamouri and Ansmann, 2016, 2017; Ansmann et al., 2019; He et al., 2025), the ICNC still exceeded the INPC by more than an order of magnitude, strongly suggesting the occurrence of SIP in the supercooled liquid layer. We define the ratio of ICNC at 180 m below the SLB to INPC at the SLT as the IMF; thus, the IMF was 36.2 during this period of 22 min (excluding 1-min radar self-check). Further, if calculated by time periods, the IMF increased from 26.3 during the first 10 min to 46.1 during the last 10 min, indicating a progressive enhancement of ice multiplication with time.

3.2 Case 2 on 3 December 2024: no significant SIP

Fig. 5 shows the stratiform MPC in 20:10-22:30 LT from lidar and MMCR observations on 3 December 2024. The supercooled liquid layer was identified to be at 4.20-4.62 km based on the joint observations of lidar and MMCR, with a colder CTT of -10.6 °C. Because the single-layer stratiform MPC was thicker in this case 2 than in the above case 1, the laser pulse could not effectively reach the cloud top height due to its rapid attenuation in the supercooled water layer.

The ice virga was mainly located between 3.12 and 4.20 km between 20:20 and 22:10 LT (marked by a rectangle in Fig. 5a-c), and the averaged BSC, VDR, and IWC during this period are presented in Fig. 6a-c. When ice crystals sedimented to approximately 120 m lower than the SLB, the mean BSC dropped sharply to 6.9 Mm^{-1} sr^{-1} from a very high value in the supercooled water layer, and the VDR increased from a minimum value of 0.08 at the SLB to a local peak of 0.17. Owing to the sublimation of ice virga during their descent, all the BSC, VDR, and IWC showed a gradually declining trend until ice virga disappeared. These characteristics are quite similar to those in case 1.

https://doi.org/10.5194/egusphere-2026-4709
Preprint. Discussion started: 2 September 2026

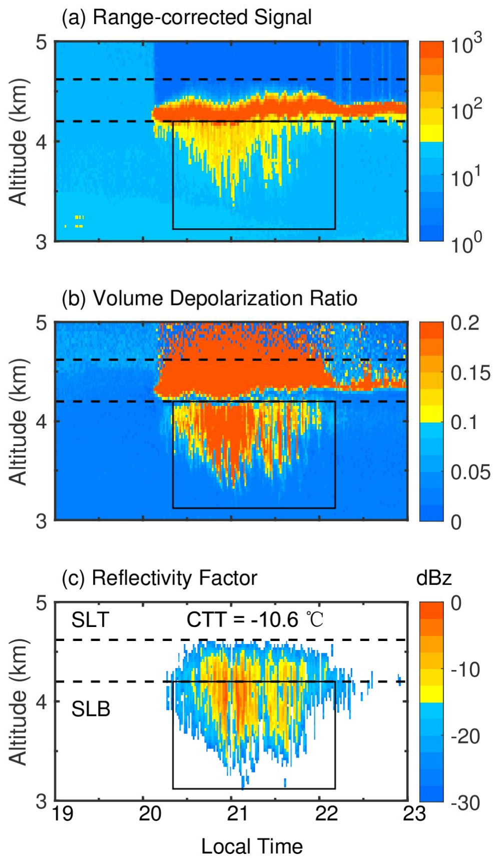

215 **Figure 5. A single-layer MPC from lidar and MMCR observations between 20:20-22:30 LT on 3 December 2024. Time-height sections of (a) RCS, (b) VDR, and (c) Z. The dashed lines represent the top and base of the supercooled liquid layer. The solid rectangles represent the ice virga region of our concern during 20:20-22:10 LT.**

https://doi.org/10.5194/egusphere-2026-4709
Preprint. Discussion started: 2 September 2026

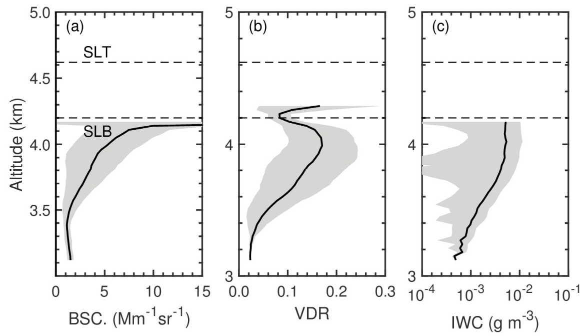

Figure 6. Profiles of averaged (a) BSC, (b) VDR, and (c) IWC in 20:20-22:10 LT. Shadows represent the values of standard deviation. The dashed lines represent the top and base of the supercooled liquid layer.

The mean VDR and PDR were derived from the lidar observation in 18:00-20:00 LT prior to the occurrence of MPC (Fig. 7a), and the mean BSC of dust and continental aerosols were obtained in this period (Fig. 7b). The BSC of dust and continental aerosols were observed with 0.29 Mm^{-1} sr^{-1} and 0.17 Mm^{-1} sr^{-1} at the height of the SLT (Fig. 7b), corresponding to the INPCd of 0.013 L^{-1} and INPCc of 0.098 L^{-1} (Fig. 7c), respectively. Given the temperature range of -8.7 °C to -10.6 °C within the supercooled liquid layer at 21:00 LT, plate-like ice crystals were applied to the ICNC retrieval. At 20:20-22:10 LT, the averaged ICNC at 180 m below the SLB was retrieved as 0.334 L^{-1} (Fig. 7c), which was approximately 3.0 times higher than the total INPC of 0.111 L^{-1}. Note that the IMF of 3.0 in this case is within the uncertainty factor (~3) for the INPC and ICNC estimation, implying that there was no significant SIP.

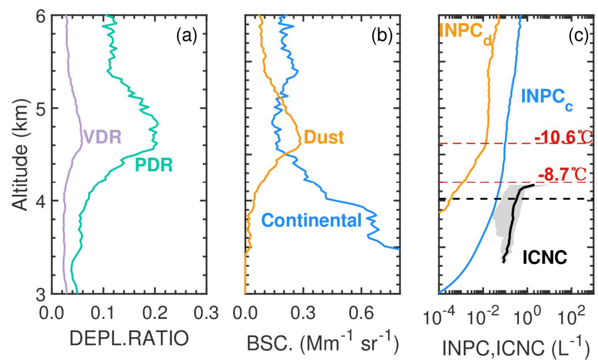

Figure 7. Profiles of (a) VDR and PDR, (b) continental and dust aerosol BSC in 18:00-20:00 LT, and (c) INPC for continental and dust aerosols in 18:00-20:00 LT and ICNC for ice virga in 20:20-22:10 LT. In Fig. 7c, the dashed horizontal black line represents the 180 m below the SLB, and the dashed horizontal red lines represent the SLT and SLB, respectively.

https://doi.org/10.5194/egusphere-2026-4709
Preprint. Discussion started: 2 September 2026

To investigate the temporal evolution of the IMF in the period, we computed the IMF over a duration of 10 min, which is presented in Fig. 8, along with the mean spectrum width (W) in the supercooled liquid layer for examining their connection. The IMF showed a trend of increasing first and then decreasing in the range of 0.6 ~ 6.0, suggesting a possible enhancement of ice production around 21:00 LT. It was interesting that the temporal variation of IMF has a similar trend to that of W, with a correlation coefficient of 0.8. Since W is generally used as an indicator of turbulence intensity (Fang et al., 2014), the large W would facilitate the formation of SIP by increasing the probability of collisions of ice-droplets or ice-ice. On the other hand, the SIP broadened the Doppler velocity spectrum, leading to an increase in W; thus, they had a high positive correlation.

It should be mentioned that the mean W of 0.12 m s^{-1} in the supercooled liquid layer was close to the value of 0.09 m s^{-1} in case 1. However, the IMF (0.6 ~ 6.0) in case 2, with temperatures of -10.6℃ to -8.7℃ in the supercooled liquid layer, was an order of magnitude lower than that (26.3-46.1) in case 1, with slightly warmer temperatures of -6.8℃ to -6.3℃. In view of the classical HM process that arises mainly between -8 ℃ and -3 ℃, the comparison suggests that temperature played a dominant role in regulating SIP processes. Therefore, case 2 provides a stark contrast to case 1, highlighting the dominant role of temperature in controlling the ice crystal multiplication.

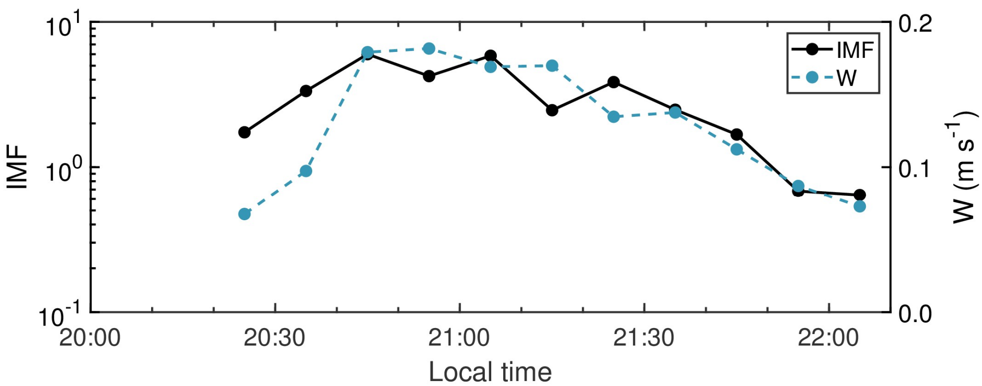

Figure 8. Evolution of 10-minute averaged IMF and W in the supercooled liquid layer.

4 Statistical characteristics of 11 cases

For the two typical cases above, the first case shows substantial SIP associated with a warmer CTT, whereas the second case exhibits no significant SIP under a colder CTT, providing a representative comparison. Similarly, we analyzed the other 9 single-layer stratiform MPCs from the joint lidar-radar observations. All 11 cases, along with their corresponding parameters, were listed in Table 1. The cloud-top height varied from 2.94 to 7.32 km, with CTT ranging from -4.9 to -

https://doi.org/10.5194/egusphere-2026-4709
Preprint. Discussion started: 2 September 2026

22.8 °C. For most cases, INPs were mainly contributed by continental aerosols, with INPCc being 1-3 orders of magnitude higher than INPCd, which agrees with earlier studies that the ice-nucleating efficiency of mineral dust may decrease at temperatures above -20 °C (Marinou et al., 2019). For the four cases (1 January 2022, 26 February 2022, 21 October 2023, 15 November 2025), there was no detectable dust contribution due to dust over Wuhan mostly concentrated below 2 km during winter (Jing et al., 2024).

Fig. 9a shows the relationship between the retrieved INPC and ICNC for each case. The INPC strongly depends on cloud-top temperature, varying by approximately two orders of magnitude from 10^0 L^{-1} (CTT= -22.8 °C) to 10^{-2} L^{-1} (CTT > -10 °C). The ICNC was estimated to be 10^{-1}-10^1 L^{-1}. For the three cases with CTT < -10 °C (21 October 2023, 24 October 2024, 3 December 2024), the ICNC was of the same order of magnitude as the corresponding INPC (blue symbols in Fig. 9a), indicating no significant SIP within the retrieval uncertainty of a factor of 3. This close agreement between INPC and ICNC in single-layer stratiform MPCs with CTT < -10 °C is consistent with the findings of an earlier study over Limassol, Cyprus (He et al., 2025), suggesting that only heterogeneous ice nucleation dominated ice formation under these relatively colder conditions. In contrast, for the remaining warmer cases (CTT >-10 °C), the ICNC exceeded the corresponding INPC by at least one order of magnitude, providing clear evidence of the involvement of SIP.

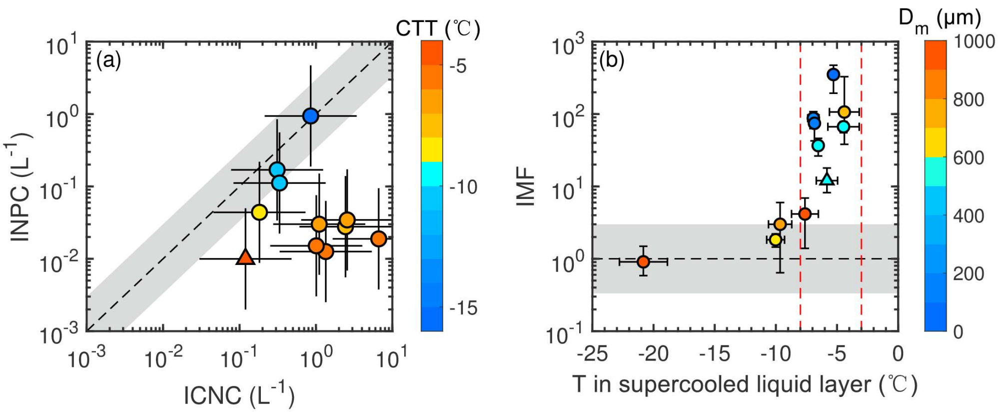

Figure 9. (a) Statistical comparison of ICNC (at 180 m below the SLB) with INPC (at the SLT) for 11 cases. Colors represent the cloud top temperature. Error bars represent the uncertainties for INPC and ICNC. (b) Statistical relationship between IMF and T in the supercooled liquid layer. Colors denote the median value of particle maximum diameters (Dm). Vertical bars represent the maximum and minimum values of 10-min average IMF in each case. Horizontal bars represent the temperature range in the supercooled liquid layer. The variation of temperature in the supercooled liquid layer for some cases was very small; thus, the horizontal bar was covered by the circle. The red dashed line denotes the temperature range from -8 ~ -3 °C. Grey shadows represent the uncertainty of a factor of 3.

https://doi.org/10.5194/egusphere-2026-4709
Preprint. Discussion started: 2 September 2026

Fig. 9b shows the variation in IMF for the 11 cases with temperature (T_{SL}) of -25 °C ~ 0 °C in the supercooled liquid layer. As T_{SL} increased to -5 °C, the IMF surged from values below 3 to a maximum of 351.8. The IMF then decreased to 106.8 and 66.8 in the two warmest cases, for which the T_{SL} reached −3 °C. Since the supercooled liquid layer contains supercooled liquid water, it can serve as a "natural laboratory" for investigating secondary ice formation. These results demonstrate that SIP is substantially enhanced in stratiform MPCs with relatively warmer cloud tops, highlighting the strong temperature dependence of SIP.

Table 1. The SLT and SLB, CTT, T_{SL}, INPCd/INPCc, IMF, and Dm at 180 m below the SLB for 11 cases.

Case type	Date	SLT (km)	SLB (km)	CTT (°C)	T_{SL} (°C)	INPCd/INPCc	IMF	Dm (μm)
CTT> -10 °C	2021.10.28	5.10	4.74	-7.4	-6.5 ~ -7.4	0.002	87.6 (63.0~107.8)	229±11
	2022.01.01	2.94	2.49	-5.5	-5.1 ~ -5.5	0	351.8 (194.1~471.8)	85±11
	2022.02.26	3.78	3.60	-6.9	-6.8 ~ -6.9	0	74.5 (42.6~100.8)	200±19
	2024.10.27	5.88	5.43	-8.7	-6.5 ~ -8.7	0.002	4.1 (1.4~6.9)	953±405
	2024.12.12	4.50	4.11	-5.6	-3.1 ~ -5.6	0.067	106.8 (38.2~327.7)	747±104
	2024.12.30	3.99	3.48	-4.9	-4.9 ~ -6.7	0.025	12.0 (8.2~17.9)	599±36
	2025.11.15	4.65	4.44	-6.8	-6.3 ~ -6.8	0	36.2 (26.3~46.1)	410±30
	2025.11.18	4.53	4.11	-5.7	-3.2 ~ -5.7	0.128	66.8 (55.2~78.5)	574±37
CTT< -10 °C	2023.10.21	5.37	5.04	-10.7	-9.3 ~ -10.7	0	1.8 (1.4~2.2)	699±89
	2024.10.24	7.32	6.99	-22.8	-18.9 ~ -22.8	0.234	0.9 (0.6~1.5)	1030±120
	2024.12.03	4.62	4.20	-10.6	-8.7 ~ -10.6	0.137	3.0 (0.6~6.0)	808±151

A special case observed on 30 December 2024 is marked by the triangle in Fig. 9. In this case, the supercooled liquid layer was embedded within a temperature inversion (not shown here), resulting in a CTT of -4.9 °C that is warmer than the cloud-base temperature (-6.7 °C). The retrieved INPC and ICNC were the lowest among all cases, with values of 0.01 L^{-1} and 0.12 L^{-1}, respectively (Fig. 9a). The corresponding IMF was only 12, substantially lower than those of the other cases with T_{SL} > -8 °C. One possible explanation is that the temperature inversion inhibited the turbulence mixing between supercooled liquid water and ice crystals, as well as the upward transport of water vapor (Hu et al., 2024), thereby suppressing ice crystal growth and SIP.

In addition, the median value of particle maximum diameter (Dm) (representing the longest axis of the particle) at 180 m below the SLB was estimated, representing the size of ice crystals that had just fallen out of the supercooled liquid layer. Dm is defined as the median value of the longest axis diameter of all the ice crystals in a detected volume. Dm values are indicated by the color scale in Fig. 9b, and the corresponding values are listed in Table 1. The Dm values are generally

https://doi.org/10.5194/egusphere-2026-4709
Preprint. Discussion started: 2 September 2026

situated between 10^2 and 10^3 µm, consistent with ice crystal diameters of ~250 µm to more than 1 mm reported from airborne in situ measurements of stratiform MPCs (Yang et al., 2020). Interestingly, IMF showed a strong negative correlation with Dm, with a Pearson correlation coefficient of -0.73. This suggests that more intense SIP is associated with smaller average crystal sizes, likely because the production of numerous secondary ice fragments shifts the particle size distribution toward smaller diameters.

Table 2. Comparison of SIP in single-layer stratiform MPC with that in previous studies.

Location	Instrument	Thickness (m)	CTT (°C)	INPC (L^{-1})	ICNC (L^{-1})	IMF range	Proposed SIP mechanism	Reference
Wuhan, China (30.5°N, 114.4°E)	Ka-band MMCR, Polarization Lidar	<450	-8.7~ -4.9	0.01~0.04	0.12~6.63	<351.8	HM process	This study
Utqiaġvik, US (71.3°N, 156.8°W)	Ka-band MMCR	~300	~-6	-	-	10^{0}~10^{2}	drizzle droplet shattering	Luke et al. (2021)
Hyytiälä, Finland (61.8°N, 24.3°E)	W-band MMCR	<500	~-3	10^{-4}~10^{1}	10^{-2}~10^{1}	10^{1}~10^{3}	-	Li et al. (2021)
Caribbean Sea, US (16°N, 64°W)	airborne in situ measurements	~400	-8	10^{-5}~10^{-4}	0.05~5	10^{3}-10^{5}	droplet collisional freezing, pre-activated INPs	Yang et al. (2020)
Svalbard, Norway (81°N, 13°E)		450	-6.5	0.006	1.43~17.8	10^{2}-10^{3}	HM process, ice-ice collisional breakup	Sotiropoulou et al. (2020)
Svalbard, Norway (81°N, 13°E)		<400	-6.7~-4.6	-	1~10	-	HM process	Raatikainen et al. (2026)

https://doi.org/10.5194/egusphere-2026-4709
Preprint. Discussion started: 2 September 2026

A comparison of the present results with those reported in previous studies is listed in Table 2. The retrieved ICNCs in this study (0.12 ~ 6.63 L^{-1}) fall within the range of previously reported values (10^{-2} ~ 10^{1} L^{-1}). The general agreement among observations from tropical, mid-latitude, and polar regions suggests that SIP in relatively warm stratiform MPCs is likely a widespread phenomenon rather than a location-specific feature. Nevertheless, no consensus has been reached regarding the dominant SIP mechanism responsible for the observed ice multiplication (Table 2). In the present study, the clear temperature dependence of the IMF is consistent with the classic HM rime-splintering process, which is active within the temperature range of approximately -8 to -3 °C (marked by the red dashed lines in Fig. 9b) and reaches its maximum efficiency around -5 °C (Hallett and Mossop, 1974; Field et al., 2017; Korolev and Leisner, 2020). Although previous studies have suggested that droplet shattering and ice-ice collisional breakup can also provide non-negligible contributions to SIP (Luke et al., 2021; Sotiropoulou et al., 2020), both observational and modeling studies indicate that these SIP mechanisms are generally most efficient at colder temperatures, typically between -20 °C and -10 °C (Korolev and Leisner, 2020). Meanwhile, recent large eddy simulations showed that the HM process is considerably more efficient than these two alternative mechanisms at temperatures warmer than -10 °C (Raatikainen et al., 2026). Therefore, our synergistic lidar-radar observations suggest that the HM process is the dominant mechanism responsible for ice multiplication in single-layer, shallow stratiform MPCs under relatively warmer conditions, although contributions from other SIP mechanisms cannot be completely excluded.

5 Conclusions

In this study, we investigated second ice production in single-layer, shallow stratiform mixed-phase cloud based on the synergistic observations from a 532-nm polarization lidar and a Ka-band millimeter cloud radar over Wuhan, China. The joint lidar-radar observations can well identify the vertical structure of a single-layer shallow stratiform MPC with a supercooled liquid-topped layer and the falling-out ice virgae below. The analysis was based on comparisons between the INPC retrieved at the cloud-top heights of cloud-free surrounding regions using the POLINPHON method, and the ICNC retrieved 180 m below the supercooled liquid base using the LIRAS-ice algorithm.

Two contrasting case studies demonstrated a distinct temperature dependence of SIP. Under a warmer T_{SL} of -6.8 ~ -6.3 °C, SIP was highly active with an average IMF of 36.2 (26.3-46.1); whereas, under a colder T_{SL} of -10.6 ~ -8.7 °C, SIP was relatively weak with an IMF of only 3.0 (0.6 ~ 6.0). Statistical analysis of all 11 identified stratiform MPC cases further confirmed this temperature dependence of SIP. For T_{SL} below -8 °C, the IMF remained close to 1, indicating good INPC-to-ICNC agreement between INPC and ICNC and suggesting that primary heterogeneous ice nucleation is dominant in ice production. In contrast, for T_{SL} above -8 °C, the IMF exhibited a unimodal dependence on T_{SL}, reaching a maximum value of 351.8 at approximately -5 °C. Additionally, IMF was negatively correlated with the Dm decreasing, with a Pearson correlation coefficient of -0.73, indicating that stronger SIP was associated with smaller ice particles above -5 °C, likely because enhanced ice fragmentation generated a larger number of smaller secondary ice particles that were broken from the

https://doi.org/10.5194/egusphere-2026-4709
Preprint. Discussion started: 2 September 2026

much larger ones. It is worth noting that the case on 30 December 2024 affected by temperature inversion suggests that stable stratification can moderately suppress SIP by inhibiting turbulence mixing within the supercooled liquid-topped layer of an MPC.

This paper provides the first quantitative joint ground-based lidar and MMCR observational studies on the IMF in single-layer shallow stratiform MPCs. Recently, Raatikainen et al. (2026) highlighted the substantial uncertainties associated with the parameterizations of the HM process in numerical models, owing to the high sensitivity of SIP to model configurations and environmental conditions. These uncertainties continue to pose a major challenge for accurately representing SIP across different atmospheric models. The observational constraints provided by the present study offer valuable insights for improving the parameterization and representation of SIP in numerical models under realistic atmospheric conditions.

Data availability

The reanalysis data used in this study are available from ERA5 (https://cds.climate.copernicus.eu/datasets, Copernicus Climate Change Service, Climate Data Store, 2025). Data from lidar and MMCR are available on reasonable request from the corresponding author (hkm@whu.edu.cn). The retrieved data for each mixed-phase cloud case, including the ICNC, INPC, IMF, SLT and SLB can be obtained via the link https://doi.org/10.5281/zenodo.21257954.

Author contributions

D.J., K.H., and Y.H. designed the research, wrote and edited the manuscript; F.Y., R.C., F.C., and H.H. contributed to discussions of the result and manuscript; D.J., R.C., and H.H. organized the observational data.

Competing interests

The authors declare no competing interests.

Disclaimer

Acknowledgements

The authors thank the colleagues who participated in the operation of the lidar system at our site. We also acknowledge the European Centre for Medium-Range Weather Forecasts (ECMWF) for providing the ERA5 reanalysis data.

Financial support

This work was supported by the National Key Research and Development Program of China (2022YFB3901800 and 2022YFF0503700), the National Natural Science Foundation of China (grant nos. 42575138, 42005101), Hubei Provincial Special Project for Central Government Guidance on Local Science and Technology Development (2025CFC003), and the Meridian Space Weather Monitoring Project (China).

References

Ansmann, A., Mamouri, R.-E., Bühl, J., Seifert, P., Engelmann, R., Hofer, J., Nisantzi, A., Atkinson, J. D., Kanji, Z. A., Sierau, B., Vrekoussis, M., and Sciare, J.: Ice-nucleating particle versus ice crystal number concentration in altocumulus and cirrus layers embedded in Saharan dust:a closure study, Atmos. Chem. Phys., 19, 15087–15115, https://doi.org/10.5194/acp-19-15087-2019, 2019.

Ávila, E. E., Castellano, N. E., Saunders, C. P. R., Bürgesser, R. E., and Aguirre Varela, G. G.: Initial stages of the riming process on ice crystals, Geophys. Res. Lett., 36, https://doi.org/10.1029/2009GL037723, 2009.

Bailey, M. P., and Hallett, J.: A comprehensive habit diagram for atmospheric ice crystals: Confirmation from the laboratory, AIRS II, and other field studies, J. Atmos. Sci., 66, 2888–2899, https://doi.org/10.1175/2009JAS2883.1, 2009.

Bühl, J., Seifert, P., Myagkov, A., and Ansmann, A.: Measuring ice- and liquid-water properties in mixed-phase cloud layers at the Leipzig Cloudnet station, Atmos. Chem. Phys., 16, 10609–10620, https://doi.org/10.5194/acp-16-10609-2016, 2016.

Bühl, J., Seifert, P., Radenz, M., Baars, H., and Ansmann, A.: Ice crystal number concentration from lidar, cloud radar and radar wind profiler measurements, Atmos. Meas. Tech., 12, 6601–6617, https://doi.org/10.5194/amt-12-6601-2019, 2019.

Cao, R., Huang, K. M., Yi, F., Fang, J. J., Zhang, Z. R., Cheng, F. Z., and Li, J.: A double bright band originating from atmospheric instability based on Ka-band radar observation at Wuhan in China, J. Geophys. Res. Atmos., 130, e2025JD044533, https://doi.org/10.1029/2025JD044533, 2025.

Cheng, C., and Yi, F.: Falling mixed-phase ice virga and their liquid parent cloud layers as observed by ground-based lidars, Remote Sens., 12, 2094, https://doi.org/10.3390/rs12132094, 2020.

https://doi.org/10.5194/egusphere-2026-4709
Preprint. Discussion started: 2 September 2026

Copernicus Climate Change Service, Climate Data Store: ERA5 hourly data on pressure levels from 1940 to present, Copernicus Climate Change Service (C3S) Climate Data Store (CDS), https://cds.climate.copernicus.eu/datasets (last access:3 August 2026), 2026.

Coutris, P., Leroy, D., Fontaine, E., and Schwarzenboeck, A.: An inverse problem approach for the retrieval of ice particle mass from in situ measurements, J. Atmos. Oceanic Technol., 34, 2457–2473, https://doi.org/10.1175/JTECH-D-17-0013.1, 2017.

DeMott, P. J., Prenni, A. J., Liu, X., Kreidenweis, S. M., Petters, M. D., Twohy, C. H., Richardson, M. S., Eidhammer, T., and Rogers, D.: Predicting global atmospheric ice nuclei distributions and their impacts on climate, Proc. Natl. Acad. Sci., 107, 11217–11222, https://doi.org/10.1073/pnas.0910818107, 2010.

DeMott, P. J., Prenni, A. J., McMeeking, G. R., Sullivan, R. C., Petters, M. D., Tobo, Y., Niemand, M., Möhler, O., Snider, J. R., Wang, Z., and Kreidenweis, S. M.: Integrating laboratory and field data to quantify the immersion freezing ice nucleation activity of mineral dust particles, Atmos. Chem. Phys., 15, 393–409, https://doi.org/10.5194/acp-15-393-2015, 2015.

Fang, J., Huang, K., Cheng, W., Zhang, Z., Cao, R., Cheng, F., and Yi, F.: Seasonal variation and vertical characteristic of cirrus clouds at a midlatitude monsoon site from Ka-band cloud radar observation, Atmos. Res., 322, 108118, https://doi.org/10.1016/j.atmosres.2025.108118, 2025.

Fang, M., Albrecht, B. A., Ghate, V. P., and Kollias, P.: Turbulence in continental stratocumulus, Part II: Eddy dissipation rates and large-eddy coherent structures, Boundary-layer Meteorol., 150, 361–380, https://doi.org/10.1007/s10546-013-9872-4, 2014.

Fernald, F. G.: Analysis of atmospheric lidar observations: some comments, Appl. Opt., 23, 652–653, https://doi.org/10.1364/AO.23.000652, 1984.

Field, P. R., Lawson, P., Brown, P., Lloyd, G., Westbrook, C., Moisseev, D., Miltenberger, A., Nenes, A., Blyth, A., Choularton, T., Connolly, P., Bühl, J., Crosier, J., Cui, Z., Dearden, C., DeMott, P., Flossmann, A. I., Heymsfield, A. J., Huang, Y., and Sullivan, S.: Secondary Ice Production: Current State of the Science and Recommendations for the Future, Meteor. Mon., 58, 7.1–7.20, https://doi.org/10.1175/AMSMONOGRAPHS-D-16-0014.1, 2017.

Freudenthaler, V., Esselborn, M., Wiegner, M., Heese, B., Tesche, M., Ansmann, A., Müller, D., Althausen, D., Wirth, M., Fix, A., Ehret, G., Knippertz, P., Toledano, C., Gasteiger, J., Garhammer, M., and Seefeldner, M.: Depolarization ratio profiling at several wavelengths in pure Saharan dust during SAMUM2006, Tellus B, 61, 165–179, https://doi.org/10.1111/j.1600-0889.2008.00396.x, 2009.

Hallett, J. and Mossop, S. C.: Production of secondary ice particles during the riming process, Nature, 249, 26–28, https://doi.org/10.1038/249026a0, 1974.

He, Y., Yin, Z., Ansmann, A., Liu, F., Wang, L., Jing, D., and Shen, H.: POLIPHON conversion factors for retrieving dust-related cloud condensation nuclei and ice-nucleating particle concentration profiles at oceanic sites, Atmos. Meas. Tech., 16, 1951–1970, https://doi.org/10.5194/amt-16-1951-2023, 2023.

He, Y., Seifert, P., Jimenez, C., Radenz, M., Ansmann, A., Bühl, J., Mamouri, R. E., Barja González, B.: Response of mixed-phase cloud microphysics to aerosol perturbations at the contrasting sites of Limassol, Cyprus, and Punta Arenas, Chile, J. Geophys. Res. Atmos., 130, e2024JD043157, https://doi.org/10.1029/2024JD043157, 2025.

Hersbach, H., Bell, B., Berrisford, P., Hirahara, S., Horányi, A., Munoz-Sabater, J., Nicolas, J., Peubey, C., Radu, R., Schepers, D., Simmons, A., Soci, C., Abdalla, S., Abellan, X., Balsamo, G., Bechtold, P., Biavati, G., Bidlot, J., Bonavita, M., De Chiara, G., Dahlgren, P., Dee, D., Diamantakis, M., Dragani, R., Flemming, J., Forbes, R., Fuentes, M., Geer, A., Haimberger, L., Healy, S., Hogan, R. J., Hólm, E., Janisková, M., Keeley, S., Laloyaux, P., Lopez, P., Lupu, C., Radnoti, G., de Rosnay, P., Rozum, I., Vamborg, F., Villaume, S., and Thépaut, J.-N.: The ERA5 global reanalysis, Q. J. Roy. Meteor. Soc., 146, 1999–2049, https://doi.org/10.1002/qj.3803, 2020.

Hersbach, H., Bell, B., Berrisford, P., Biavati, G., Horányi, A., Muñoz Sabater, J., Nicolas, J., Peubey, C., Radu, R., Rozum, I., Schepers, D., Simmons, A., Soci, C., Dee, D., Thépaut, J.-N.: ERA5 hourly data on pressure levels from 1940 to present,] Copernicus Climate Change Service (C3S) Climate Data Store (CDS) [data set], https://doi.org/10.24381/cds.bd0915c6, 2023.

Hogan, R. J., Mittermaier, M. P., and Illingworth, A. J.: The retrieval of ice water content from radar reflectivity factor and temperature and its use in evaluating a mesoscale model, J. Appl. Meteorol. Clim., 45, 301–317, https://doi.org/10.1175/JAM2340.1, 2006.

Hu, X., Hou, S., Yang, J., Zhao, S., Zhang, X., Tao, Y., LI, H., Zhang, X., and Huang, H.: Microphysical Characteristics of Melting Layers in North China Revealed by Aircraft and Radar, Remote Sens., 16, 2120, https://doi.org/10.3390/rs16122120, 2024.

Jing, D., He, Y., Yin, Z., Liu, F., and Yi, F.: Long-term characteristics of dust aerosols over central China from 2010 to 2020 observed with polarization lidar. Atmos. Res., 297, 107129, https://doi.org/10.1016/j.atmosres.2023.107129, 2024.

Jing, D., He, Y., Yin, Z., Huang, K., Liu, F., and Yi, F.: Evolution of tropospheric aerosols over central China during 2010–2024 as observed by lidar, Atmos. Chem. Phys., 25, 17047–17067, https://doi.org/10.5194/acp-25-17047-2025, 2025.

Kong, W. and Yi, F.: Convective boundary layer evolution from lidar backscatter and its relationship with surface aerosol concentration at a location of a central China megacity, J. Geophys. Res. Atmos., 120, 7928–7940, https://doi.org/10.1002/2015JD023248, 2015.

Korolev, A., McFarquhar, G., Field, P. R., Franklin, C., Lawson, P., Wang, Z., Williams, E., Abel, S. J., Axisa, D., Borrmann, S., Crosier, J., Fugal, J., Krämer, M., Lohmann, U., Schlenczek, U., Schnaiter, M., and Wendisch, M.: Mixed-phase clouds: Progress and challenges, Meteorol. Monogr., 58, 5-1, https://doi.org/10.1175/AMSMONOGRAPHS-D-17-0001.1, 2017.

Korolev, A., Heckman, I., Wolde, M., Ackerman, A. S., Fridlind, A. M., Ladino, L. A., Lawson, R. P., Milbrandt, J., and Williams, E.: A new look at the environmental conditions favorable to secondary ice production, Atmos. Chem. Phys., 20, 1391–1429, https://doi.org/10.5194/acp-20-1391-2020, 2020.

https://doi.org/10.5194/egusphere-2026-4709
Preprint. Discussion started: 2 September 2026

Korolev, A. and Leisner, T.: Review of experimental studies of secondary ice production, Atmos. Chem. Phys., 20, 11767–11797, https://doi.org/10.5194/acp-20-11767-2020, 2020.

Li, H., Möhler, O., Petäjä, T., and Moisseev, D.: Two-year statistics of columnar-ice production in stratiform clouds over Hyytiälä, Finland: environmental conditions and the relevance to secondary ice production, Atmos. Chem. Phys., 21, 14671–14686, https://doi.org/10.5194/acp-21-14671-2021, 2021.

Luke, E. P., Yang, F., Kollias, P., Vogelmann, A. M., and Maahn, M.: New insights into ice multiplication using remote-sensing observations of slightly supercooled mixed-phase clouds in the Arctic, Proc. Natl. Acad. Sci., 118, e2021387118, 2021.

Marinou, E., Tesche, M., Nenes, A., Ansmann, A., Schrod, J., Mamali, D., Tsekeri, A., Pikridas, M., Baars, H., Engelmann, R., Voudouri, K.-A., Solomos, S., Sciare, J., Groß, S., Ewald, F., and Amiridis, V.: Retrieval of ice-nucleating particle concentrations from lidar observations and comparison with UAV in situ measurements, Atmos. Chem. Phys., 19, 11315–11342, https://doi.org/10.5194/acp-19-11315-2019, 2019.

Mamouri, R. E. and Ansmann, A.: Estimated desert-dust ice nuclei profiles from polarization lidar: methodology and case studies, Atmos. Chem. Phys., 15, 3463–3477, https://doi.org/10.5194/acp-15-3463-2015, 2015.

Mamouri, R. E. and Ansmann, A.: Potential of polarization lidar to provide profiles of CCN- and INP-relevant aerosol parameters, Atmos. Chem. Phys., 16, 5905–5931, https://doi.org/10.5194/acp-16-5905-2016, 2016.

Mamouri, R. E. and Ansmann, A.: Potential of polarization/Raman lidar to separate fine dust, coarse dust, maritime, and anthropogenic aerosol profiles, Atmos. Meas. Tech., 10, 3403–3427, https://doi.org/10.5194/amt-10-3403-2017, 2017.

Mao, Z., Huang, K., Fang, J., Zhang, Z., Cao, R., and Yi, F.: An Observation of Precipitation during Cooling with Ka-Band Cloud Radar in Wuhan, China, Remote Sens., 15, 5397, https://doi.org/10.3390/rs15225397, 2023.

Müller, D., Ansmann, A., Mattis, I., Tesche, M., Wandinger, U., Althausen, D., and Pisani, G.: Aerosol-type-dependent lidar ratios observed with Raman lidar, J. Geophys. Res. Atmos., 112, https://doi.org/10.1029/2006JD008292, 2007.

O'Connor, E. J., Illingworth, A. J., and Hogan, R. J.: A technique for autocalibration of cloud lidar, J. Atmos. Ocean. Tech., 21, 777–786, https://doi.org/10.1175/1520-0426(2004)021<0777:ATFAOC>2.0.CO;2, 2004.

Raatikainen, T., Calderón, S., Järvinen, E., Prank, M., and Romakkaniemi, S. Can rime splintering explain the ice production in Arctic mixed-phase clouds? Atmos. Chem. Phys. 26, 5019–5038, 2026.

Seifert, P., Ansmann, A., Müller, D., Wandinger, U., Althausen, D., Heymsfield, A. J., Massie, S. T., and Schmit, C.: Cirrus optical properties observed with lidar, radiosonde, and satellite over the tropical Indian Ocean during the aerosol-polluted northeast and clean maritime southwest monsoon, J. Geophys. Res. Atmos., 112, D17205, https://doi.org/10.1029/2006JD008352, 2007.

Shen, H., Yin, Z., He, Y., Ansmann, A., Zhan, Y., Wang, L., and Jing, D.: Impact of Asian dust on cirrus formation over the central Pacific: CALIOP-and cloudsat-observation-based case studies, J. Geophys. Res. Atmos., 129, e2024JD041265, https://doi.org/10.1029/2024JD041265, 2024.

https://doi.org/10.5194/egusphere-2026-4709
Preprint. Discussion started: 2 September 2026

Sotiropoulou, G., Sullivan, S., Savre, J., Lloyd, G., Lachlan-Cope, T., Ekman, A. M. L., and Nenes, A.: The impact of secondary ice production on Arctic stratocumulus, Atmos. Chem. Phys., 20, 1301–1316, https://doi.org/10.5194/acp-20-1301-2020, 2020.

Storelvmo, T., and Tan, I.: The Wegener-Bergeron-Findeisen process–Its discovery and vital importance for weather and climate, Meteorol. Z., 24, 455–461, https://doi.org/10.1127/metz/2015/0626, 2015.

Strangeways, I.: Precipitation: Theory, measurement and distribution, Cambridge: Cambridge University Press, ISBN 9780521851176, 2006.

Tesche, M., Ansmann, A., Müller, D., Althausen, D., Engelmann, R., Freudenthaler, V., and Groß, S.: Vertically resolved separation of dust and smoke over Cape Verde using multiwavelength Raman and polarization lidars during Saharan Mineral Dust Experiment 2008, J. Geophys. Res. Atmos., 114, D13202, https://doi.org/10.1029/2009JD011862, 2009.

Wang, Z., Wang, H., Dong, X., Yang, Y., Ke, Y., Liu, S., Cui, Y., Cui, K., Wu, Z., and Lin, W.: Aircraft observation of aerosol and mixed-phase cloud microphysical over the North China Plain, China: Vertical distribution, size distribution, and effects of cloud seeding in two-layered clouds, Atmos. Res., 312, 107758, https://doi.org/10.1016/j.atmosres.2024.107758, 2024.

Wieder, J., Ihn, N., Mignani, C., Haarig, M., Bühl, J., Seifert, P., Engelmann, R., Ramelli, F., Kanji, Z. A., Lohmann, U., and Henneberger, J.: Retrieving ice-nucleating particle concentration and ice multiplication factors using active remote sensing validated by in situ observations, Atmos. Chem. Phys., 22, 9767–9797, https://doi.org/10.5194/acp-22-9767-2022, 2022.

Yang, J., Wang, Z., Heymsfield, A. J., DeMott, P. J., Twohy, C. H., Suski, K. J., and Toohey, D. W.: High ice concentration observed in tropical maritime stratiform mixed-phase clouds with top temperatures warmer than -8 C, Atmos. Res., 233, 104719, https://doi.org/10.1016/j.atmosres.2019.104719, 2020.

Yi, Y., Yi, F., Liu, F., Zhang, Y., Yu, C., and He, Y.: Micro-physical process of precipitating hydrometeors from warm front mid-level stratiform clouds revealed by ground-based lidar observations, Atmos. Chem. Phys., 21, 17649–17664, https://doi.org/10.5194/acp-21-17649-2021, 2021.

Yi, Y., Yi, F., Huang, K., Liu, F., Zhang, Y., Yu, C., He, Y., and Yin, Z.: Locally formed thin supercooled liquid stratiform clouds on mid-level moisture advection layers as observed by ground-based lidars, radar, and radiosondes at a subtropical site, J. Geophys. Res. Atmos., 129, e2024JD041405, https://doi.org/10.1029/2024JD041405, 2024.

Zhang, Z., Huang, K., Yi, F., Cheng, W., Liu, F., Zhang, J., and Jia, Y.: Technical note: Evolution of convective boundary layer height estimated by Ka-band continuous millimeter wave radar at Wuhan in central China, Atmos. Chem. Phys., 25, 3347–3361, https://doi.org/10.5194/acp-25-3347-2025, 2025.